Equilibrium bridge solution from a sessile drop partially covered by another fluid

P. D. Ravazzoli ⬤, A. G. González ⬤, and J. A. Diez ⬤

*Instituto de Física Arroyo Seco, Universidad Nacional del Centro de la Provincia de Buenos Aires
and CIFICEN-CONICET-CICPBA, Pinto 399, 7000 Tandil, Argentina*

We study the equilibrium solutions of a fluid bridge that connects a horizontal solid substrate with a fluid phase (typically, air) while surrounded by another immiscible liquid. The shape of each interface is considered as a single curve with axial symmetry and constant curvature. The interface between the bridge and the air phase is a spherical cap, while the one between the external liquid and the air has zero curvature. Finally, the liquid-liquid interface corresponds to portions of onduloids or nodoids. The equilibrium solution must satisfy the boundary conditions given by Neumann's at the three fluids junction (triple point) and Young's law at the two fluids-solid contact line (at the substrate). For given fluids, we find that the solution control parameter is the γ angle, which is the slope of the surrounding interface respect to the horizontal at the triple point. Using this procedure, we are able to find the γ regions where different kinds of solutions are possible. In order to assess which solution is more likely to be found in nature, we compare their surface energies looking for that corresponding to the lowest one. Finally, we find numerical solutions that consider the presence of a vessel wall containing the fluids, by using the analytical results to provide guess values needed to initiate the required iterative process.

I. INTRODUCTION

The knowledge of a drop shape when it is surrounded by other immiscible liquids and/or in contact with solid bodies is a subject that has always raised interest in fluids mechanic [1]. A nonexhaustive list of examples includes the shapes of a sessile drop under different wettability conditions on a solid substrate [2] as well as on another liquid [3–6], or that of a fluid bridge that connects two solid surfaces such as disks or rings [7–13]. The solution of these basic problems, even if they seem to have only an academic appeal, can lead to the development of new techniques to manipulate tiny droplets with application in several fields of industry [14–16].

All of the above-mentioned configurations involve two fluids (usually a liquid and a gas) and a solid substrate. The inclusion of another liquid phase has also raised interest in the literature [17,18], as it is the case of compound or multiphase drops. These are comprised of two (or more) immiscible fluid drops that share an interface with one another, surrounded by a third immiscible fluid. Such drops exist in several areas, such as multiphase processing, biological interactions within cells, and atmospheric chemistry. While in the previous cases, the solid substrate does not play a crucial role in determining the equilibrium shapes, it is essential in a four-phases configuration, consisting of two liquids, one gas, and a solid, such as the one studied here.

We consider a sessile drop of fluid A with volume $\mathcal{V}_A$ that rests on planar solid, which is partially surrounded by a fluid B, so that the contact angle at substrate is θ_s. The top of the sessile drop is in contact with another fluid C (see Fig. 1). All fluids are immiscible and, at least, two of them must
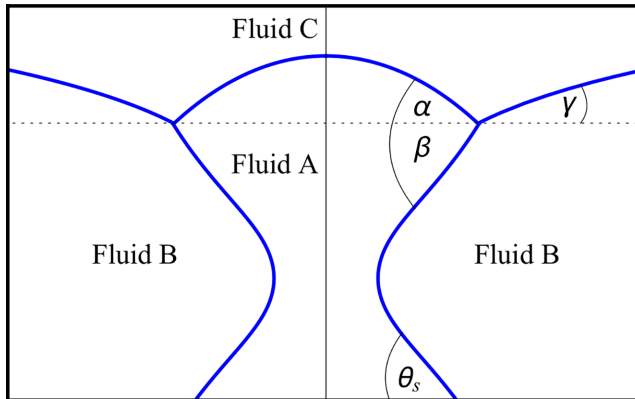
FIG. 1. Schemes of the fluid bridge of volume $\mathcal{V}_A$ that connects the solid substrate with the free surface. The configuration has symmetry of revolution around the central axis.

be liquids. Here, we focus on finding the static equilibrium configuration, and not on the dynamics of the evolution towards it.

The paper is organized as follows. In Sec. II, we formulate the basic problem in a nondimensional way, and we describe the mathematical procedure used to determine the equilibrium solutions for the three surfaces. In Sec. III, we analyze different types of solutions showing their characteristics, number of necks, and their corresponding variations in angle γ. Since, for some specific values of γ, there are several solutions, we evaluate and compare the surface energies associated with each one of them, looking for the one with minimum energy. In Sec. IV, we analyze the effects related to the wettability of the substrate by considering a wide range of contact angles, θ_s. In Sec. V, we present numerical results for the problem with boundary walls for fluid B. Section VI is devoted to summarize the results and discuss their implications.

II. FORMULATION OF THE PROBLEM

In order to obtain a relatively simple equilibrium solution, we restrict our study to axial symmetry so that each surface, $\mathcal{S}$, can be reduced to a single curve in the r-z plane. A schematical shape is depicted in Fig. 2. Curve 1 corresponds to $\mathcal{S}_{AC}$ (surface of the interface between fluids A and C), curve 2 to $\mathcal{S}_{AB}$ and curve 3 to $\mathcal{S}_{BC}$. At the solid substrate, we consider that curve 2 has a contact angle θ_s, which depends on the degree of wettability of the solid by fluid A when surrounded by fluid B. We also use $\mathcal{S}_{AS}$ and $\mathcal{S}_{BS}$ to denote the contact surfaces between fluids A and B, respectively, with the substrate S.

At equilibrium, the angles (α, β, γ) at the triple point (A-B-C) of coordinates (r_*, z_*) (see Fig. 2) must satisfy Neumann's conditions

$$\alpha + \beta = \arccos\left(\frac{\sigma_1^2 - \sigma_2^2 - \sigma_3^2}{2\sigma_3\sigma_2}\right), \quad \alpha + \gamma = \pi - \arccos\left(\frac{\sigma_2^2 - \sigma_3^2 - \sigma_1^2}{2\sigma_3\sigma_1}\right), \tag{1}$$

where the subscripts in the surface tensions, σ's, account for the corresponding interface. The scheme in Fig. 2 shows these angles when they are positive. In the special case of a floating lens (i.e., when fluid A does not touch the substrate) on a liquid B of infinite extension [6,19], we have $\gamma = 0$. If the lens were in contact with the substrate, the interface BC would no longer be flat and then $\gamma \neq 0$ at the triple point. As we will discuss later, the value of γ defines the shape of the equilibrium solutions. It can be shown that the relations in Eq. (1) can be satisfied if the surface tensions satisfy [6]

$$-2\min(\sigma_1, \sigma_2) < S = \sigma_3 - \sigma_1 - \sigma_2 < 0, \tag{2}$$
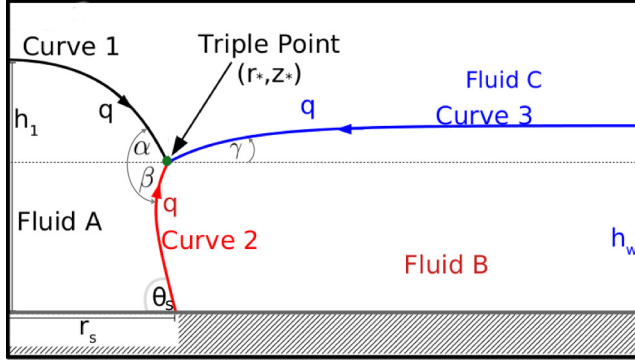
FIG. 2. Scheme of the equilibrium solution: A fluid bridge (curve 2) connects the triple point (r_*, z_*) with the solid substrate where the contact angle is θ. Curve 1 corresponds to the interface between the upper part of fluid A and fluid C while curve 3 is the interface between fluids B and C. The arrows indicate the increasing direction of the arc length, q. The angles α, β, and γ are positive in this scheme.

where S is the spreading parameter of A laying on B and surrounded by C. The minimum value of S assures that the angles (α, β, γ) can actually be computed, while its maximum value ($S = 0$) implies that these angles are null (i.e., A spreads indefinitely over B). Then, under these constraints, the force balances at the triple point in the horizontal and vertical directions are

$$\sigma_1 \cos \alpha + \sigma_2 \cos \beta - \sigma_3 \cos \gamma = 0, \tag{3a}$$

$$\sigma_1 \sin \alpha - \sigma_2 \sin \beta + \sigma_3 \sin \gamma = 0. \tag{3b}$$

Each curve, representing the interfaces, is defined by the Laplace pressure jump condition:

$$\Delta p_i = \sigma_i \kappa_i = \sigma_i \left(\frac{1}{\mathcal{R}_{\parallel,i}} + \frac{1}{\mathcal{R}_{\perp,i}} \right), \tag{4}$$

where κ_i is the curvature of the ith curve and $\mathcal{R}_{\parallel,i}$ and $\mathcal{R}_{\perp,i}$ are the curvature radii in the r-z plane and in the perpendicular plane that contains the normal to the curve i at the point, respectively. Besides, the pressure equilibrium implies that the sum of the pressure jumps, $\Delta p_i = \sigma_i \kappa_i$ at the three interfaces, must be zero, so that

$$\sigma_1 \kappa_1 + \sigma_2 \kappa_2 + \sigma_3 \kappa_3 = 0. \tag{5}$$

Note that these curvatures are constant along the curves, since gravity effects are neglected.

We define the radius of a spherical shape of volume $\mathcal{V}_A$

$$\mathcal{R}_0 = \left(\frac{3 \mathcal{V}_A}{4\pi} \right)^{1/3} \tag{6}$$

as a characteristic length, where

$$\mathcal{V}_A = \int_0^{z_*} \pi r_2(z_2)^2 \, dz_2 + \int_{z_*}^{z_1(r_1=0)} \pi r_1(z_1)^2 \, dz_1. \tag{7}$$

As a consequence, the dimensionless volume of fluid A is $V_A = 4\pi/3$.

Also, by considering σ_1 as the reference surface tension, we define the following dimensionless ratios:

$$\eta = \frac{\sigma_2}{\sigma_1}, \quad \zeta = \frac{1}{2} \left(1 + \eta - \frac{\sigma_3}{\sigma_1} \right). \tag{8}$$

Thus, the restrictions in Eq. (2) imply

$$\eta > 0, \qquad 0 < \zeta < \min(1, \eta). \tag{9}$$

Therefore, Eqs. (3a), (3b), and (5), can be written in dimensionless form as

$$\cos\alpha + \eta\cos\beta - (1 + \eta - 2\zeta)\cos\gamma = 0, \tag{10a}$$

$$\sin\alpha - \eta\sin\beta + (1 + \eta - 2\zeta)\sin\gamma = 0, \tag{10b}$$

$$\kappa_1 + \eta\kappa_2 + (1 + \eta - 2\zeta)\kappa_3 = 0, \tag{10c}$$

where the κ_i's are now in units of $\mathcal{R}_0$.

In order to obtain the shape of each curve, we have to solve [6,19]

$$\kappa_i = \frac{z_i'}{r_i\left(1 + z_i'^2\right)^{1/2}} + \frac{z_i''}{\left(1 + z_i'^2\right)^{3/2}} = \text{const.,} \tag{11}$$

where $z_i = z_i(r)$ and prime stands for d/dr_i. Since the curve 3 extends to infinity, we consider [see Eq. (5)],

$$\kappa_3 = 0, \quad \Rightarrow \quad \kappa_1 = -\frac{\sigma_2}{\sigma_1}\kappa_2 = -\eta\kappa_2. \tag{12}$$

In the following, we proceed to calculate the solutions for each curve with curvatures κ_i, $i = 1, 2, 3$.

A. Solution for curve 1

In this case, since the curve passes through the symmetry axis, we have $R_{\parallel,1} = R_{\perp,1} \equiv R_1$, so that $\kappa_1 = 2/R_1$. Its value is given by

$$\kappa_1 = \frac{2\sin\alpha}{r_*}, \tag{13}$$

where r_* is the radius of the triple point (see Fig. 1). Therefore, curve 1 corresponds to the circumference

$$z_1 = \left[\left(\frac{r_*}{\sin\alpha}\right)^2 - r_1^2\right]^{1/2} + z_d, \tag{14}$$

where z_d is to the vertical displacement of the center of the spherical cap needed to meet the circumference with the other two curves at (r_*, z_*).

B. Solution of curve 3

By considering both Eqs. (11) and (12), the ordinary differential equation (ODE) for curve 3 takes the form:

$$\frac{z_3''}{1 + z_3'^2} = -\frac{z_3'}{r_3}. \tag{15}$$

This equation can be easily integrated to yield:

$$\frac{\psi}{\sqrt{1 + \psi^2}} = \frac{\lambda_1}{r_3}, \tag{16}$$

where λ_1 is a constant and $\psi = z_3'$. Solving for ψ, we have

$$\psi = \frac{dz_3}{dr_3} = \frac{\lambda_1}{\sqrt{r_3^2 - \lambda_1^2}}. \tag{17}$$

Here, we have taken the positive square root, so that the sign of λ_1 determines that of ψ. By performing a second integration, we find

$$z_3 = \lambda_1 \ln\left(r_3 + \sqrt{r_3^2 - \lambda_1^2}\right) + \lambda_2, \tag{18}$$

with $\lambda_2 = \text{const}$. Note that this equation can be inverted to:

$$r_3 = \lambda_1 \cosh\left(\frac{z_3 - \lambda_3}{\lambda_1}\right), \tag{19}$$

where $\lambda_3 = \lambda_2 + \lambda_1 \ln \lambda_1$. Thus, the shape of curve 3 is that of a catenary. In the triple contact point, (r_*, z_*), we have $\psi = \tan\gamma$, so that the constants are given by:

$$\lambda_1 = r_* \sin\gamma,$$

$$\lambda_2 = z_* - r_* \sin\gamma \ln\left[r_*(1 + \cos\gamma)\right] = z_* - r_*\text{ArgCosh}\left(\frac{1}{\sin\gamma}\right). \tag{20}$$

As a result, we observe that the shape of curve 3 is determined for given (r_*, z_*, γ), as well as that of curve 1, since both α and β depend on γ [see Eq. (3)]. Therefore, we focus now on obtaining curve 2, which together with curve 1 enclose the dimensionless volume of fluid A, $V_A = 4\pi/3$.

C. Solution for curve 2

In order to calculate curve 2, it is convenient to rewrite Eq. (11) in terms of its slope defined as

$$z_2' = \frac{dz_2}{dr_2} = -\tan\theta. \tag{21}$$

Thus, we obtain

$$\cos\theta \frac{d\theta}{dr_2} + \frac{\sin\theta}{r_2} = -\kappa_2, \tag{22}$$

or equivalently,

$$\frac{1}{r_2} \frac{d}{dr_2}(r_2 \sin\theta) = -\kappa_2. \tag{23}$$

By using Eqs. (5), (8), and (13) with $\kappa_3 = 0$, we have

$$\frac{1}{r_2} \frac{d}{dr_2}(r_2 \sin\theta) = \frac{2}{\eta} \frac{\sin\alpha}{r_*}. \tag{24}$$

Upon integration, we find

$$r_2 \sin\theta = \frac{1}{\eta} \frac{r_2^2 \sin\alpha}{r_*} + C_1, \tag{25}$$

where C_1 is an integration constant. This solution can be written as a quadratic expression for $x = r_2/r_*$ as

$$x^2 - \eta \frac{\sin\theta}{\sin\alpha} x + \eta \frac{C_1}{r_* \sin\alpha} = 0. \tag{26}$$

Note that this is an ODE for $x(y)$ with $y = z_2/r_*$. In fact [see Eq. (21)],
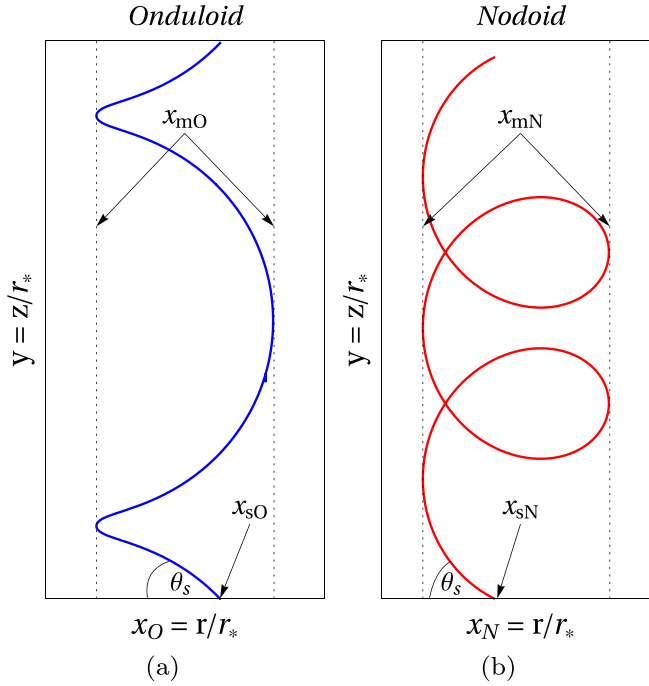
$$\sin\theta = \frac{1}{\sqrt{1 + x'^2}}, \tag{27}$$

FIG. 3. Typical shapes for real and positive values of x_m and x_s: (a) onduloid, (b) nodoid. The final solution that fulfills the boundary conditions is given by a portion of these curves.

where $x' = dx/dy$. For each sign of the square root, we obtain a different ODE for $x(y)$, namely,

$$x^2 \pm \frac{\eta}{\sin\alpha} \frac{x}{\sqrt{1+x'^2}} + \eta \frac{C_1}{r_* \sin\alpha} = 0. \tag{28}$$

Interestingly, the solution of this equation is an onduloid, $x_O(y)$, for the minus sign, and a nodoid, $x_N(y)$, for the plus sign [20]. Schematic representations of these types of curves are shown in Fig. 3.

In order to calculate C_1, we apply the boundary condition at the substrate:

$$\theta = \theta_s \quad at \quad x = x_s, \tag{29}$$

where $x_s = r_s/r_*$. Thus, from Eq. (26) we have (including the two possible signs):

$$C_1 = \frac{r_* \sin\alpha}{\eta} x_s \left(-x_s \pm \eta \frac{\sin\theta_s}{\sin\alpha} \right), \tag{30}$$

and, consequently, the quadratic expressions for both the onduloid, $x_O(y)$, and the nodoid, $x_N(y)$, are (see Fig. 3):

$$x_O \left(x_O - \eta \frac{\sin\theta}{\sin\alpha} \right) - x_{sO} \left(x_{sO} - \eta \frac{\sin\theta_s}{\sin\alpha} \right) = 0, \tag{31a}$$

$$x_N \left(x_N + \eta \frac{\sin\theta}{\sin\alpha} \right) - x_{sN} \left(x_{sN} + \eta \frac{\sin\theta_s}{\sin\alpha} \right) = 0. \tag{31b}$$

These equations must also be satisfied at the other extreme of the curve 2, namely, the triple contact point, where $x_N = x_O = 1$ and $\theta = \pi - \beta$:

$$\left(1 - \eta \frac{\sin \beta}{\sin \alpha}\right) - x_{sO}\left(x_{sO} - \eta \frac{\sin \theta_s}{\sin \alpha}\right) = 0, \tag{32a}$$

$$\left(1 + \eta \frac{\sin \beta}{\sin \alpha}\right) - x_{sN}\left(x_{sN} + \eta \frac{\sin \theta_s}{\sin \alpha}\right) = 0. \tag{32b}$$

The roots of these quadratic equations yield the values of x_{sO} and x_{sN} for each type of solution. Both α and β are determined by Eqs. (10a) and (10b), and can be considered functions of γ for given values of the parameters η and ζ. Therefore, these roots are determined solely by the pair (θ_s, γ). Moreover, the solutions (either onduloid or nodoid) can exist only for both real and positive values of x_{sO} and x_{sN}.

Interestingly, the solution $x(y)$ may have turning points (i.e., maximum or minimum x values) as it connects the extremes $x = x_s$ and $x = 1$. The x coordinates of these points, x_m, are given by the condition $\sin \theta = 1$, and they satisfy:

$$x_{mO}\left(x_{mO} - \frac{\eta}{\sin \alpha}\right) - x_{sO}\left(x_{sO} - \eta \frac{\sin \theta_s}{\sin \alpha}\right) = 0, \tag{33a}$$

$$x_{mN}\left(x_{mN} + \frac{\eta}{\sin \alpha}\right) - x_{sN}\left(x_{sN} + \eta \frac{\sin \theta_s}{\sin \alpha}\right) = 0. \tag{33b}$$

Thus, x_{mO} and x_{mN} can be obtained after x_{sO} and x_{sN} have been calculated from Eq. (32). In Fig. 3, we show the characteristic shape of onduloids and nodoids bounded by the x_m values. Note that only a portion of the onduloid or nodoid will be of interest to build up curve 2.

Finally, the expression for the ODE of the onduloid (nodoid) can be obtained by replacing Eq. (27) and Eq. (32a) [Eq. (32b)] into Eq. (31a) [Eq. (31b)], and solving for x'_O (x'_N). Thus, we have

$$z_O = r_* y_O = r_* \int_{x_{sO}}^{x} \frac{dx}{x'_O} = r_* \int_{x_{sO}}^{x} \frac{\eta \sin \beta + (x^2 - 1) \sin \alpha}{\sqrt{(\eta x)^2 - [\eta \sin \beta + (x^2 - 1) \sin \alpha]^2}} dx, \tag{34a}$$

$$z_N = r_* y_N = r_* \int_{x_{sN}}^{x} \frac{dx}{x'_N} = r_* \int_{x_{sN}}^{x} \frac{\eta \sin \beta - (x^2 - 1) \sin \alpha}{\sqrt{(\eta x)^2 - [\eta \sin \beta - (x^2 - 1) \sin \alpha]^2}} dx, \tag{34b}$$

which can also be written in terms of elliptical integrals of the first and second kind. The resulting expressions are quite cumbersome, we solve them numerically. As we will see below, they must be restricted to z intervals where the slope $x(z)$ is monotonously increasing or decreasing.

In Fig. 4, we schematically show the possible shapes for x_s smaller, larger and between the x_m values. If $x_m < x_s$, two solutions exist: one with $\beta < 90°$ that presents a neck [blue line in Fig. 4(a)], while the other with $\beta > 90°$ does not [red line in Fig. 4(a)]. For $x_{m1} < x_s < x_{m2}$ [see Fig. 4(b)], curve 2 is bounded by two turning points, so that onduloids can have different number of necks. Finally, for $x_s < x_m$ [see Fig. 4(c)], there are solutions only for $\beta > 90°$.

III. EQUILIBRIUM SOLUTIONS

In order to obtain the full equilibrium solution of a fluid bridge, we need to characterize the fluids involved in the problem by giving η and ζ (i.e., the relations between the surface tensions of the three fluids), as well as the wettability of the solid substrate, the contact angle, θ_s. Once these parameters are given, Eqs. (31)–(33) determine the γ intervals where solutions can exist, i.e., where x_s is real and positive. Despite the fact that they can be found for all γ within $(-180°, 180°)$, here we focus only $0° \leqslant \gamma \leqslant 90°$, since this is the γ range where curve 3 (the catenary) is physically meaningful.
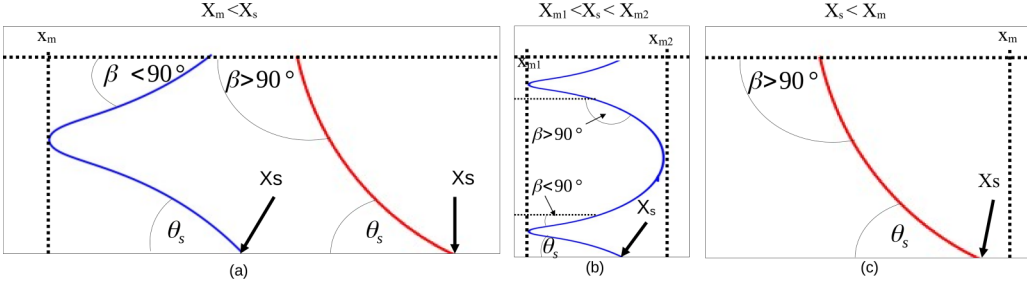
FIG. 4. Schemes of possible shapes of curve 2 (onduloid or nodoid) for real and positive values of x_m and x_s. (a) For $x_m < x_s$, two solutions are possible depending on angle β at the triple point. For $\beta < 90°$, it is given by the blue curve, which connects x_s with the triple contact point through a neck. Instead, for $\beta > 90°$, it is given by the red curve which is shorter than the blue one and monotonously connects x_s with the triple point. (b) For $x_{m1} < x_s < x_{m2}$, the solution is bounded by x_{m1} and x_{m2} (see Fig. 3). The conditions at the triple point ($x = 1$) can be satisfied at different y's, which are determined by the value of β. (c) For $x_s < x_m$, the solution must be monotonous so that the only possibility is to meet the triple contact point with $\beta > 90°$, analogously to the red curve in (a).

In Fig. 5, we show the positive roots x_s and x_m for both onduloids [Fig. 5(a)] and nodoids [Fig. 5(b)] as a function of γ for $(\eta, \zeta, \theta_s) = (0.8, 0.2, 45°)$. In the case of the onduloid, it can be seen in Fig. 5(a) that the solutions do no exist within the interval $7.29° < \gamma < 26.75°$ (gray zone), where real and positive x_{sO}'s cannot be found. Instead, Fig. 5(b) shows that no nodoid solution exists for $40.81° < \gamma < 70.30°$ (gray zone), where real and positive x_{sN}'s can neither be found. Interestingly, both types of solutions exist in γ regions where Eqs. (31a) and (31b) yield at least one real and positive root. By combining the results shown in Figs. 5(a) and 5(b) (see the vertical lines), we summarize the types of possible solutions for each γ in Table I.

For given γ, it is possible to find the complete shape of the fluid bridge by solving Eqs. (14) and (34). In Fig. 6, we show the solutions for $\gamma = 3°, 30°, 38°$, and $75°$ (see Table I). These values correspond to regions where three equilibrium solutions are possible. On the one hand, Figs. 6(a) and 6(b) show the cases for γ smaller than the asymptotic value $\gamma = 34°$ where two onduloids and
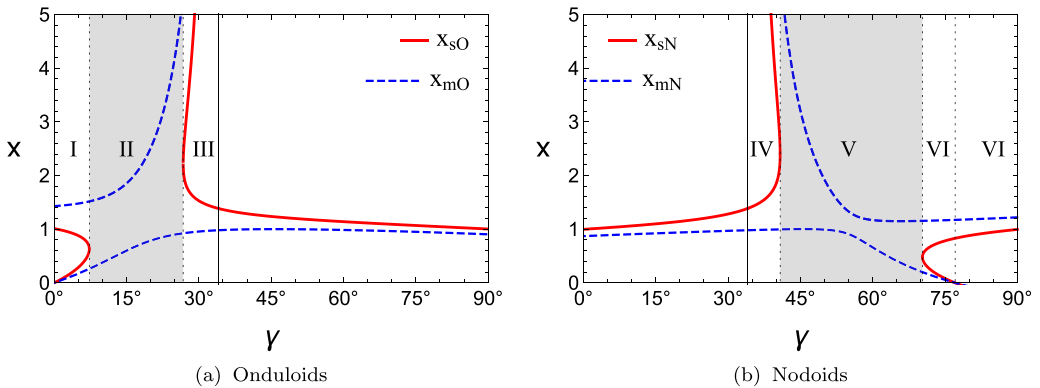

FIG. 5. Radius of the foot bridge, $x_s = r_s/r_*$, and radius with vertical slope, $x_m = r_m/r_*$, in units of the triple point radius, as a function of γ (see Fig. 2) for $(\eta, \zeta, \theta_s) = (0.8, 0.2, 45°)$. (a) Onduloids: There is no solution for $\gamma < 0$ since $x_{mO} > x_{sO}$ as well as for $7.9° < \gamma < 26.7°$ (between dashed lines) because x_{sO} is not real and positive. (b) Nodoids: There is no solution for $40.8° < \gamma < 70.3°$ because x_{sN} is not real and positive. Both the vertical solid lines (asymptotes of the curves) and the dashed lines are the borders of the γ regions indicated in Table I.

TABLE I. Types of solutions within intervals of the angle γ for $(\eta, \zeta, \theta_s) = (0.8, 0.2, 45°)$.

Zone	γ interval	Solutions	In Fig. 6
I	$(0°, 7.9°)$	2 onduloids, 1 nodoid	(a) $\gamma = 3°$
II	$(7.9°, 26.7°)$	1 nodoid	
III	$(26.7°, 34°)$	2 onduloids, 1 nodoid	(b) $\gamma = 30°$
IV	$(34°, 40.8°)$	1 onduloid, 2 nodoids	(c) $\gamma = 38°$
V	$(40.8°, 70.3°)$	1 onduloid	
VI	$(70.3°, 77.1°)$	1 onduloid, 2 nodoids	(d) $\gamma = 75°$
VII	$(77.1°, 90°)$	1 onduloid	

one nodoid can occur. On the other hand, Figs. 6(c) and 6(d) show two nodoids and one onduloid that can exist for $\gamma > 34°$. It should be mentioned that, for $60.35° < \gamma < 90°$, the curve 1 with the onduloid touches the bottom ($z = 0$) before reaching the symmetry axis and, therefore, it does not have physical meaning. This fact can be seen in Fig. 6(d) at z_O^b (black line) for $\gamma = 75°$, so that this onduloid (even if it exists) is meaningful only for $\gamma < 60.35°$. Nevertheless, we still have two valid solutions of the nodoid type corresponding to zone VI in Table I.
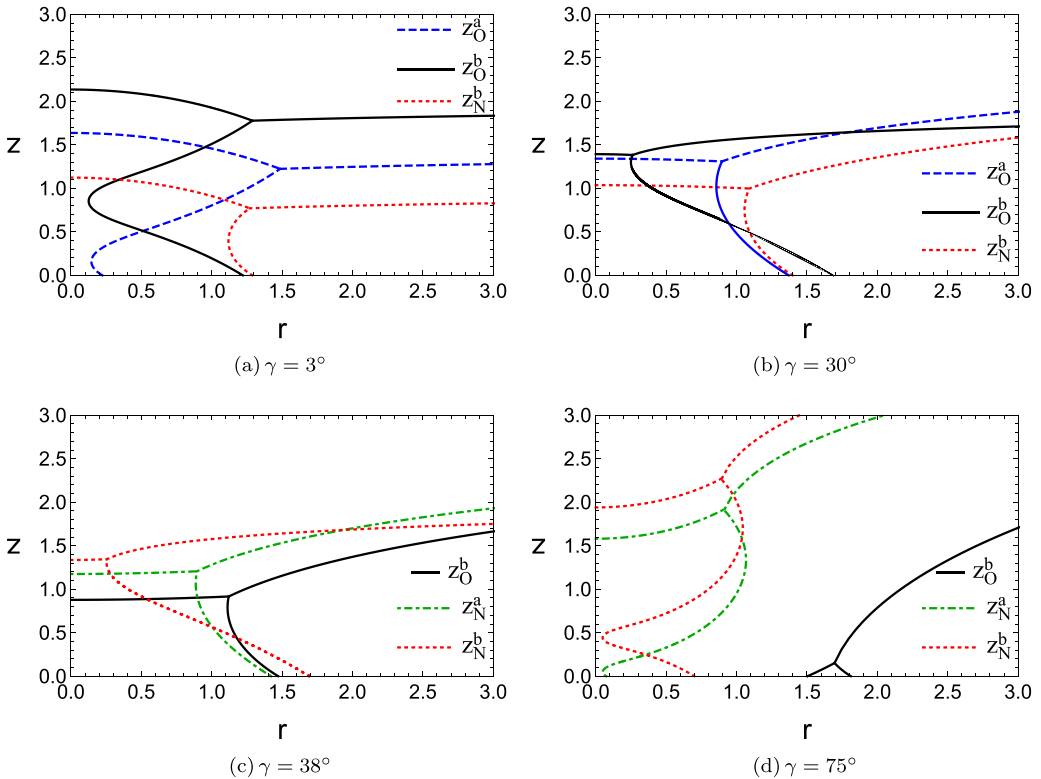

FIG. 6. Equilibrium solutions for $(\eta, \zeta, \theta) = (0.8, 0.2, 45°)$ and different values of γ (see Table I). (a) Zone I, $\gamma = 3°$ ($\alpha = 31.05°$; $\beta = 47.41°$), (b) Zone III, $\gamma = 30°$ ($\alpha = 4.05°$; $\beta = 74.41°$), (c) Zone IV, $\gamma = 38°$ ($\alpha = -3.95°$; $\beta = 82.41°$), (d) Zone VI, $\gamma = 75°$ ($\alpha = -40.95°$; $\beta = 119.41°$). In (a) and (b), we have two onduloids (z_O^a and z_O^b) and one nodoid (z_N^b). In (c) and (d), we have one onduloid (z_O^b) and two nodoids (z_N^a and z_N^b).
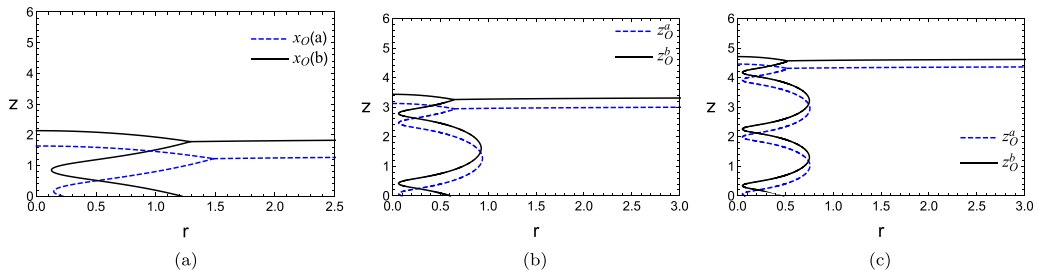
FIG. 7. Different equilibrium solutions for the same set of physical parameters $(\eta, \zeta, \theta) = (0.8, 0.2, 45°)$ and $\gamma = 3°$. Onduloid solutions for: (a) one neck, (b) two necks, and (c) three necks.

Furthermore, if γ is within a region where $0 < x_{mO,1} < x_{sO} < x_{mO,2}$, several periods of the onduloid may occur before it reaches the triple point, $x = 1$. As one considers an increasing number of periods, i.e., more necks, the solution must become narrower and higher due to the conservation of the bridge volume An example of this case is shown in Fig. 7 for $\gamma = 3°$. On the contrary, this kind of periodic construction cannot be performed with the nodoids since it would require to include regions with loops [see Fig. 3(b)].

A. Energetic analysis

As noticed in the previous sections, it is possible to obtain different solutions for the shape of the bridge depending on the value of γ for given (η, ζ, θ_s). Here, we consider the surface energy of each solution, since we expect that the one with the lowest energy is more likely to be observed in nature. Therefore, we focus only on one neck solutions, since a higher number of necks increases the bridge surface, and consequently, its energy.

The surface energy of the bridge can be calculated as:

$$\mathcal{E}_b = \sigma_1 \mathcal{S}_{AC} + \sigma_2 \mathcal{S}_{AB} + \sigma_4 \mathcal{S}_{AS} + \sigma_0 (\mathcal{S}_S - \mathcal{S}_{AS}) + \sigma_3 \mathcal{S}_{BC}, \qquad (35)$$

where σ_0 and σ_4 are the fluid B substrate and fluid A substrate surface tensions, respectively, and $\mathcal{S}_S$ is the area of the substrate surface.

In order to define a reference energy, we consider a configuration consisting of a single drop of fluid A sitting on the substrate and completely covered by fluid B, so that its energy is given by

$$\mathcal{E}_0 = \sigma_1 \mathcal{S}_d + \sigma_4 \mathcal{S}'_d + \sigma_0 (\mathcal{S}_S - \mathcal{S}'_d) + \sigma_3 \mathcal{S}_S, \qquad (36)$$

where $\mathcal{S}_d$ and $\mathcal{S}'_d$ stand for the free and footprint surfaces of the fluid A drop, respectively. Therefore, the net energy of the bridge is

$$\Delta \mathcal{E} = \mathcal{E}_b - \mathcal{E}_0 = \sigma_1 (\mathcal{S}_{AC} - \mathcal{S}_d) + \sigma_2 [\mathcal{S}_{AB} - \cos \theta_s (\mathcal{S}_{AS} - \mathcal{S}'_d)] + \sigma_3 (\mathcal{S}_{BC} - \mathcal{S}_S), \qquad (37)$$

where we have used Young's law:

$$\cos \theta_s = \frac{\sigma_0 - \sigma_4}{\sigma_2}. \qquad (38)$$

In dimensionless form, we have

$$\Delta E = \frac{\Delta \mathcal{E}}{\sigma_1 \mathcal{R}_0^2} = (S_{AC} - S_d) + \eta [S_{AB} - \cos \theta_s (S_{AS} - S'_d)] + (1 + \eta - 2\zeta)(S_{BC} - S_S), \qquad (39)$$
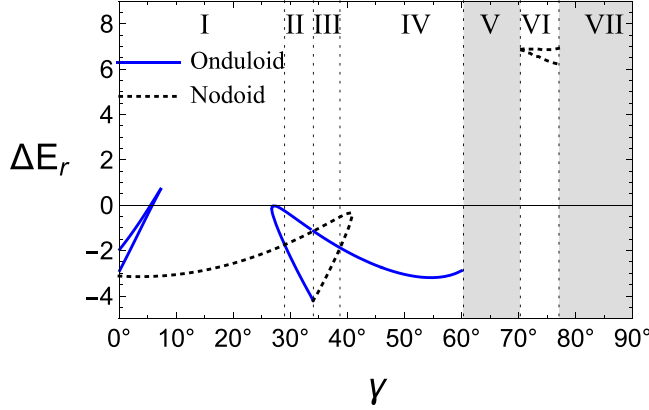
FIG. 8. Capillary energy of the bridge, ΔE_r, as a function of the angle γ. The solid vertical lines separate the zones named in Table II. The minimum energy solution as γ increases is a nodoid [black line, $(0°, 29°)$, zone I], an onduloid [blue line, $(29°, 34°)$, zone II], a nodoid [black line, $(34°, 38.7°)$, zone III], an onduloid [blue line, $(38.7°, 60.35°)$, zone IV], a nodoid [black line, $(70.3°, 77.1°)$, zone VI]. There is no solution with physical meaning in zones V $(60.35°, 70.3°)$, and VII $(77.1°, 90°)$.

where

$$S_{AC} = 2\pi r_*^2 \frac{1 - \cos \alpha}{\sin \alpha}, \quad S_{AS} = \pi r_s^2, \quad S_d = 2\pi r_d^2 \frac{1 - \cos \theta_s}{\sin \theta_s}, \qquad S_d' = \pi r_d^2, \qquad (40)$$

$$S_{BC} = \int_{r_*}^{r_w} 2\pi r \left(1 + z_3'^2\right)^{1/2} dr, \qquad S_S = \pi r_w^2, \qquad (41)$$

r_w is the radius of the vessel (wall) containing the fluids, and

$$r_d = \frac{2 \cos (\theta_s/2)}{[\sin (3\theta_s/2)]^{1/3}} \qquad (42)$$

is the fluid A sessile drop radius.

The surface S_{BC} in Eq. (41) turns out to be:

$$S_{BC} = \pi \left[r_w^2 \delta(r_w) - r_*^2 \delta(r_*)\right] + \log \left[\frac{r_w}{r_*} \frac{1 + \delta(r_w)}{1 + \delta(r_*)}\right] \pi r_*^2 \sin^2 \gamma, \qquad (43)$$

where

$$\delta(r) = \sqrt{1 - \frac{r_*^2}{r^2} \sin^2 \gamma}, \qquad (44)$$

Note that $S_{BC} - S_S$ in Eq. (39) gives $-\pi r_*^2$ for $\gamma = 0$. However, for $\gamma \neq 0$ and $r_w \to \infty$, this difference is not finite but diverges logarithmically, even if S_{BC}/S_S tends to one for $r_w \to \infty$. This means that, even if the slope z_3' in Eq. (41) decreases as $1/r_w$, the area S_{BC} increases for large r_w. Therefore, we will not consider the last term in Eq. (43), which accounts for the divergence in order to preserve the information about the energy of the bridge surfaces. Instead, we retain only the first term, so that $S_{BC} - S_S \to -\pi r_*^2 \cos \gamma$ for $r_w \to \infty$. Thus, the definition of the reduced system difference energy is

$$\Delta E_r = (S_{AC} - S_d) + \eta[S_{AB} - \cos \theta_s (S_{AS} - S_d')] - (1 + \eta - 2\zeta)\pi r_*^2 \cos \gamma. \qquad (45)$$

In Fig. 8 we show $\Delta E_r(\gamma)$ for $0 \leqslant \gamma \leqslant 90°$ where different regions can be observed. The gray regions correspond to onduloid solutions that have $z_1 < 0$, which invalidates them, so that $\Delta E_r(\gamma)$ is not calculated for these γ ranges. Note also that the onduloid and nodoid solutions for $\gamma = 34°$

TABLE II. Lowest-energy solutions in the interval $0° \leqslant \gamma \leqslant 90°$ for $(\eta, \zeta, \theta_s) = (0.8, 0.2, 45°)$.

	γ interval	Lowest-energy solution
I	$(0°, 29°)$	nodoid
II	$(29°, 34°)$	onduloid
III	$(34°, 38.7°)$	nodoid
IV	$(38.7°, 60.35°)$	onduloid
V	$(60.35°, 70.3°)$	no solution
VI	$(70.3°, 77.1°)$	nodoid
VII	$(77.1°, 90°)$	no solution

[at the asymptote of $x(y)$ in Fig. 5] are coincident, and therefore, have the same energy. In Table II, we indicate the type of solution with the lowest energy for each γ region.

In order to determine if the lowest-energy solution is prone to be unstable under perturbations, a stability analysis would be required, analogously to what was done for bridges between axisymmetric bodies [21]. This task is out of the scope of the present work.

IV. EFFECTS RELATED WITH DIFFERENT CHOICES OF THE PARAMETERS

In the previous section, we have focused our attention on obtaining detailed solutions for a set of parameters (η, ζ, θ_s). Here, we consider the effects of varying the wetting conditions at the substrate as given by the contact angle, θ_s. As shown above, the existence of solutions is basically determined by the fact that positive real values of x_s can be found. Moreover, the shapes of the solutions depend on the relation between x_m, x_s and θ_s.

Different θ_s's define the γ regions where the solutions are possible. In Fig. 9, we show x_s and x_m as a function of γ for both the onduloid and the nodoid solutions by considering some values of $\theta_s < 90°$. Blue lines correspond to $x_m(\gamma)$ and red ones to $x_s(\gamma, \theta_s)$, while arrows indicate the increasing direction of θ_s. Interestingly, for $\theta_s = 60°$ both roots of x_s [see Eq. (32)] are coincident and this fact corresponds to the crossing point of the red curves in Fig. 9. For $\theta_s > 60°$, the red curves $x_s(\gamma, \theta_s)$ approach to the blue lines $x_m(\gamma)$, and are coincident for $\theta_s = 90°$.
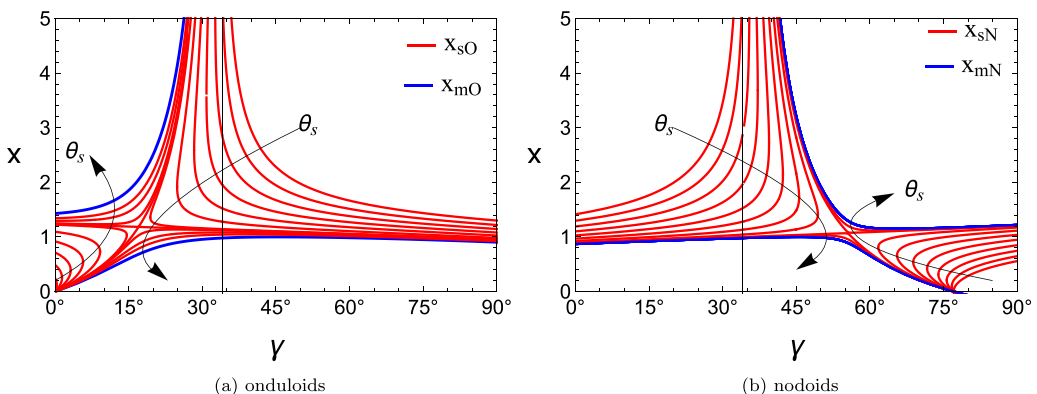

FIG. 9. Effects of contact angle, θ_s, for $(\eta, \zeta) = (0.8, 0.2)$. The blue lines correspond to $x_m(\gamma)$ and the red ones to $x_s(\gamma, \theta_s)$ for $0 < \theta_s < 90°$. (a) Onduloids and (b) nodoids. The arrows indicate the increasing direction of θ_s for $\theta_s = 0°, 10°, 20°, 30°, 40°, 50°, 59°, 60°, 61°, 65°, 70°, 90°$. In particular, for $\theta_s = 60°$ both roots of x_s [see Eq. (32)] are coincident and corresponds to the crossing point of the red curves.

TABLE III. Boundary conditions for the six equations in Eq. (46).

	Curve 1	Curve 2	Curve 3
$r(q_i = 0)$	0	r_s	r_w
$r'(q_i = 0)$	L_1	$-L_2 \cos \theta_s$	$-L_3$
$z(q_i = 0)$	h_1	0	h_w
$z'(q_i = 0)$	0	$L_2 \sin \theta_s$	0

As indicated in Fig. 4, the relation between x_s and x_m is a key issue in order to assert which type of solution is to be found (onduloid or nodoid), before performing the integration of Eq. (34). Therefore, Fig. 9 allows us to determine the values of x_s and x_m for given γ and θ_s. The same procedure applies when parameters like η or ζ are changed.

V. NUMERICAL SOLUTION

The previous analytical solution is very helpful to describe all possible configurations when gravity is negligible. Moreover, it constitutes a good starting point to analyze more complex situations, as we will discuss in this section. However, it has some drawbacks that must be borne in mind. In fact, the imposed zero curvature of surface 3 implies an unbounded height as radius increases. Therefore, this solution does not take into account the finite size of the vessel containing the liquids. Another drawback of the present analytical solution is that it precludes the addition of gravity effects, which requires surfaces of nonconstant curvature. In order to overcome these issues, one must resort to numerical methods to solve the complete problem. Here, we present numerical results for the problem within a finite vessel and leave for future work the inclusion of gravity effects.

The methodology is a modified version of that we used for liquid lenses in Ref. [6]. It consists of an iterative scheme that solves six coupled nonlinear second-order ODE's and their corresponding 12 boundary conditions with nine unknown constants to be consistently determined. The main physical differences between the analytical and numerical approaches are that the constant curvatures of each surface are free parameters to be determined in the numerical case, and that curve 3 has zero slope at a fixed and large enough value of r. The latter is equivalent to a 90° contact angle at the distant wall of the containing vessel, $r = r_w$.

The expressions of Eq. (11), which give the Laplace (capillary) pressure jumps along the curves 1, 2, and 3 in terms of $z_i(r_i)$, can be written [6,19] in a parametric form as

$$r_i''(q_i) = z_i'(q_i) \left[\frac{z_i'(q_i)}{r_i(q_i)} - L_i \Delta P_i \right], \tag{46a}$$

$$z_i''(q_i) = -r_i'(q_i) \left[\frac{z_i'(q_i)}{r_i(q_i)} - L_i \Delta P_i \right], \tag{46b}$$

where $[r_i(q_i), z_i(q_i)]$ are the dimensionless cylindrical coordinates in units of $\mathcal{R}_0$ and $\Delta P_i = \mathcal{R}_0 \Delta p_i / \sigma_i$ are the dimensionless pressure jumps. Here, $q_i = s/L_i$ is the scaled arc length along the curves, where s is the arc length and L_i is the dimensionless total arc length of the ith curve. Consequently, we have

$$L_i^2 = r_i'(q_i)^2 + z_i'(q_i)^2 = \text{const.} \tag{47}$$

Since we define $q_i = 1$ at the triple point where all curves meet and end up, the point where they begin corresponds to $q_i = 0$. Note that the coordinates $[r_i(0), z_i(0)]$ are $(0, h_1)$ for curve 1, $(r_s, 0)$ for curve 2, and (r_w, h_w) for curve 3 (see Fig. 2).

In Table III, we summarize the 12 boundary conditions needed for the integration of the six second-order differential equations in Eq. (46). However, these equations have six unknowns,

namely, three ΔP_i's and three L_i's. Moreover, the conditions listed in Table III add the following three additional parameters: r_s, h_1, and h_w, while the contact angle θ_s is given. Therefore, we have nine unknowns in total:

$$\mathcal{U} = (\Delta P_1, \Delta P_2, \Delta P_3, L_1, L_2, L_3, r_s, h_w, h_1), \tag{48}$$

so that we need nine constraints to solve the problem.

The first four constraints come from the fact that all three curves must meet at the triple point of coordinates (r_*, z_*). Thus, we have

$$r_* = r_1(q_1 = 1) = r_2(q_2 = 1) = r_3(q_3 = 1), \tag{49a}$$

$$z_* = z_1(q_1 = 1) = z_2(q_2 = 1) = z_3(q_3 = 1). \tag{49b}$$

Other three constraints are given by the slopes of the curves at $q = 1$, as:

$$\frac{dz_1}{dr_1} = -\tan\alpha, \qquad \frac{dz_2}{dr_2} = \tan\beta, \qquad \frac{dz_3}{dr_3} = \tan\gamma. \tag{50}$$

The last two conditions come from the pressure balance, Eq. (10c), and the volume conservation of fluid A, which in dimensionless and parametric form is [see Eq. (7)],

$$V_A = \pi \left(\int_0^1 r_2^2 z_2' dq_2 + \int_0^1 r_1^2 z_1' dq_1 \right) = \frac{4\pi}{3}. \tag{51}$$

Therefore, the problem can be completely solved by means of Eqs. (10c), (49)–(51) for given values of η, ζ, θ, γ, and r_w.

In order to obtain the solution, we develop an algorithm that numerically integrates Eq. (46) by using Runge-Kutta methods inside a Newton-Raphson routine that iteratively changes the set of parameters $\mathcal{U}$ in Eq. (48) to satisfy all the constraints. This procedure requires to start the iteration with a guess value of $\mathcal{U}$. The analytical solution, $r_i(z_i)$ or $z_i(r_i)$, obtained in the previous sections provides a good starting point for this initial guess. In fact, for given η, ζ, θ_s, γ, and r_w we obtain:

$$\begin{aligned}
&\Delta P_1 = -\kappa_1, & &L_1 = r_* \alpha_l / \sin\alpha_l, & &r_s = r_2(z_2 = 0), \\
&\Delta P_2 = \eta\kappa_2, & &L_2 = \tilde{L}_2, & &h_w = z_3(r_3 = r_w), \\
&\Delta P_3 = \epsilon, & &L_3 = r_w - r_*, & &h_1 = z_1(r_1 = 0),
\end{aligned} \tag{52}$$

where $\tilde{L}_2$ is the length of curve 2 of the analytical solution. We typically use $\epsilon = 10^{-5}$ and $r_w = 30$. Since several solutions may be possible for given $(\eta, \zeta, \theta_s, \gamma)$ (see Table I), we must consider their corresponding set of guess values.

In Fig. 10, we show the analytical and numerical solutions for $(\eta, \zeta, \theta, \gamma) = (0.8, 0.2, 45°, 3°)$, where it can be seen that they are very similar for both the onduloid and nodoid case. The main differences are observed in curve 3 where the zero slope condition at $r = r_w$ in the numerical solution generates a slight change of its shape. We also note that, despite being small, the numerical curvature κ_3 is not strictly zero. These differences are a consequence of the addition of the constraints at the wall. If the wall is sufficiently far from the bridge, they are small enough to be neglected.

Note that the numerical solution yields a finite V_B for given r_w. Therefore, this volume of fluid B should be used in an experiment if one wishes to obtain the same solution for the same r_w. Conversely, for arbitrary values of V_B and r_w, no solution might exist for the problem. This may happen when there are no analytical solutions for certain γ ranges (see Table I), as we have actually checked in our own numerical scheme since it does not converge.
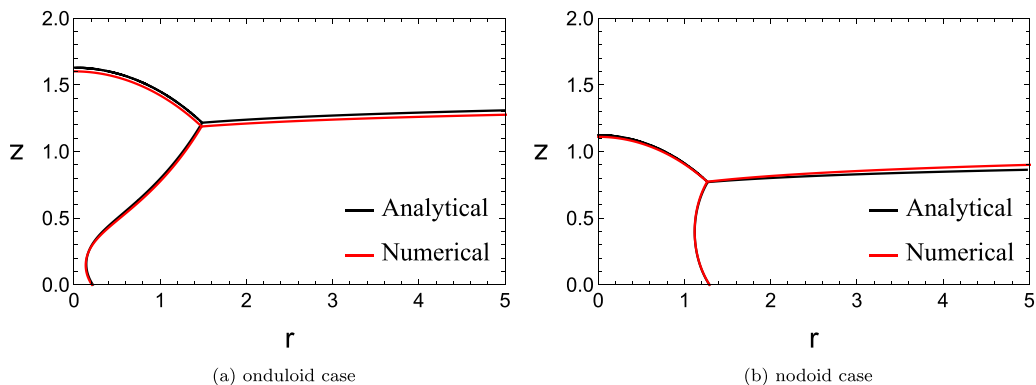
FIG. 10. Comparison between numerical and analytical solutions for $(\eta, \zeta, \theta, \gamma) = (0.8, 0.2, 45°, 3°)$: (a) onduloid case and (b) nodoid case. The main differences between the solutions are in curve 3 because the numerical solution is obtained with a finite volume of fluid B as well as with $dz/dr = 0$ at $r = r_w = 30$.

VI. SUMMARY AND CONCLUSIONS

In this work, we obtain families of equilibrium solutions for the problem of a fluid volume $\mathcal{V}_A$ in contact with a solid substrate and partially emerging from a surrounding immiscible fluid B, while a third one, C, completely covers both of them. These solutions are obtained analytically from the physical constraints given by the Neumann's equilibrium equations, the matching of all three curves at the triple point, the wetting condition at the substrate and the conservation of volume $\mathcal{V}_A$.

We show that the solution is determined by four parameters, namely: (i) the ratios of two surface tensions η, (ii) the spreading factor, ζ, (iii) the contact angle at the solid substrate, θ_s, and (iv) the γ angle at the triple contact point. Only γ is neither determined by the type of liquids nor the solid substrate, so that it becomes the control parameter of the problem. In particular, the analytical equilibrium solution is composed by a spherical cap for curve 1, a catenary for curve 3, and either an onduloid or a nodoid for curve 2. Interestingly, we find that several solutions coexist for the same set of physical parameters and the same γ in some cases, while in others, there is no solution at all.

Through a first integration of the governing equations and applying the boundary conditions, we are able to determine which kind of solutions are possible for given γ. This is done by comparing the relative positions of the solid contact line, r_s, the turning points of curve 2, r_m, and the triple contact line, r_*. Thus, we were able to perform the second integration to obtain the final shape of curve 2. We also calculate the surface energy of the solutions in order to assert which one is more likely to be observed in nature when more than one theoretical solution can be found. We consider the effects of changing the solid substrate wettability by varying θ_s and describe a graphical methodology to infer which kind of solution is to be obtained, before performing the second integration of the ODE's.

Finally, we implement an algorithm with an iteration procedure that numerically solves the six coupled equations with more realistic boundary conditions, such as a real vessel containing the fluids and a 90° contact angle at the vessel border. We implement an iterative scheme leading to a converged numerical solution that uses the analytical results for the infinite vessel as a starting guess. We find that there no significant differences between them when the vessel radius is sufficiently large. Looking forward, we plan to use this numerical scheme to approach more complex scenarios where gravity effects are taken into account, since they can be included straightforwardly in the scheme.

ACKNOWLEDGMENTS

[1] H. M. Princen and S. G. Mason, Shape of a fluid drop at a fluid-liquid interface II: Theory for three-phase systems, J. Colloid Sci. **20**, 246 (1965).

[2] P. G. de Gennes, Wetting: statics and dynamics, Rev. Mod. Phys. **57**, 827 (1985).

[3] Y. Seeto, J. E. Puig, L. E. Scriven, and H. T. Davis, Interfacial tensions in systems of three liquid phases, J. Colloid Interface Sci. **96**, 360 (1983).

[4] F. B. Wyart, P. Martin, and C. Redon, Liquid/liquid dewetting, Langmuir **9**, 3682 (1993).

[5] K. Takamura, N. Loahardjo, W. Winoto, J. Buckley, N. R. Morrow, M. Kunieda, Y. Liang, and T. Matsuoka, Spreading and retraction of spilled crude oil on sea water, in *Crude Oil Exploration in the World* (IntechOpen, Rijeka, 2012), Chap. 6.

[6] P. D. Ravazzoli, A. G. González, J. A. Diez, and H. A. Stone, Buoyancy and capillary effects on floating liquid lenses, Phys. Rev. Fluids **5**, 073604 (2020).

[7] A. Borkar and J. Tsamopoulos, Boundary-layer analysis of the dynamics of axisymmetric capillary bridges, Phys. Fluids A **3**, 2866 (1991).

[8] J. W. van Honschoten, N. R. Tas, and M. Elwenspoek, The profile of a capillary liquid bridge between solid surfaces, Am. J. Phys. **78**, 277 (2010).

[9] F. M. Orr, L. E. Scriven, and A. P. Rivas, Pendular rings between solids: meniscus properties and capillary force, J. Fluid Mech. **67**, 723 (1975).

[10] B. J. Lowry and P. H. Steen, Capillary surfaces: Stability from families of equilibria with application to the liquid bridge, Proc. R. Soc. Lond. A **449**, 411 (1995).

[11] L. A. Slobozhanin, J. I. D. Alexander, and A. H. Resnick, Bifurcation of the equilibrium states of a weightless liquid bridge, Phys. Fluids **9**, 1893 (1997).

[12] B. Mielniczuk, O. Millet, G. Gagneux, and M. S. El Youssoufi, Characterisation of pendular capillary bridges derived from experimental data using inverse problem method, Granular Matter **20**, 14 (2018).

[13] H. N. G. Nguyen, O. Millet, and G. Gagneux, Liquid bridges between a sphere and a plane - classification of meniscus profiles for unknown capillary pressure, Math. Mech. Solids **24**, 3042 (2019).

[14] S. Kumar, Liquid transfer in printing processes: Liquid bridges with moving contact lines, Annu. Rev. Fluid Mech. **47**, 67 (2015).

[15] D. Lohse and X. Zhang, Surface nanobubbles and nanodroplets, Rev. Mod. Phys. **87**, 981 (2015).

[16] B. D. Gates, Q. Xu, M. Stewart, D. Ryan, C. G. Willson, and G. M. Whitesides, New approaches to nanofabrication: molding, printing, and other techniques, Chem. Rev. **105**, 1171 (2005).

[17] M. J. Neeson, R. F. Tabor, F. Grieser, R. R. Dagastine, and D. Y. C. Chan, Compound sessile drops, Soft Matter **8**, 11042 (2012).

[18] Y. Zhang, D. Chatain, S. L. Anna, and S. Garoff, Stability of a compound sessile drop at the axisymmetric configuration, J. Colloid Interface Sci. **462**, 88 (2016).

[19] J. C. Burton, F. M. Huisman, P. Alison, D. Rogerson, and P. Taborek, Experimental and numerical investigation of the equilibrium geometry of liquid lenses, Langmuir **26**, 15316 (2010).

[20] I. M. Mladenov and M. Hadzhilazova, *The Many Faces of Elastica*, Forum for Interdisciplinary Mathematics, Book 3 (Springer, Berlin, 2017).

[21] L. G. Fel and B. Y. Rubinstein, Stability of axisymmetric liquid bridges, Z. Angew. Math. Phys. **66**, 3447 (2015).